Bulletin of Electrical Engineering and Informatics
Vol. 15, No. 1, February 2026, pp. 827~844
ISSN: 2302-9285, DOI: 10.11591/eei.v15i1.9161

CT-based lung cancer detection using spatially localized integral transforms with U-NET classification

Abel Belay Wossene[1], Dawit Assefa[2], Ayodeji Olalekan Salau[3,4], Sepiribo Lucky Braide[5], Aitizaz Ali[6], Ting Tin Tin[7]
[1]Department of Biomedical Engineering, Institute of Technology, Hawassa University, Hawassa, Ethiopia
[2]School of Biomedical Engineering, College of Technology and Built Environment, Addis Ababa University, Addis Ababa, Ethiopia
[3]Department of Electrical/Electronics and Computer Engineering, Afe Babalola University, Ado-Ekiti, Nigeria
[4]Saveetha School of Engineering, Saveetha Institute of Medical and Technical Sciences, Chennai, India
[5]Department of Electrical and Electronics Engineering, Rivers State University, Port Harcourt, Nigeria
[6]School of IT, UNITAR International University, Petaling Jaya, Malaysia
[7]Faculty of Data Science and Information Technology, INTI International University, Nilai, Malaysia

Article Info

Article history:

Received Dec 13, 2024
Revised Oct 15, 2025
Accepted Dec 6, 2025

Keywords:

Feature extraction
Lung cancer
MATLAB
Spatially-localized integral transform
U-NET

ABSTRACT

Lung cancer remains the leading cause of cancer-related mortality worldwide, emphasizing the need for early, accurate, and scalable detection methods. Low-dose computed tomography (LDCT) has improved early diagnosis, yet challenges like image noise, low contrast, and subtle nodule features often limit reliable interpretation in large-scale screening. This paper proposes a computationally efficient computer-aided detection (CADe) framework that integrates a rotation-invariant, spatially localized integral transform feature extraction with a U-Net-based classifier to enhance lung nodule detection and segmentation. The approach strengthens spatial feature representation while maintaining low computational and memory demands, enabling real-time use in resource-limited clinical settings. Implemented in MATLAB and evaluated on the Cancer Imaging Archive (TCIA) dataset, the system achieved 99.32% classification accuracy, 88.88% specificity, 84.21% precision, 87.3% intersection over union (IoU), and 92.9% dice similarity coefficient (DSC). These results show clear improvements over conventional methods, particularly in rotational robustness and efficiency—key requirements for scalable screening. Although precision and IoU could be further optimized, the framework demonstrates strong potential for clinical adoption. By providing accurate, fast, and robust nodule analysis, this work advances practical high-performance tools for early lung cancer detection, especially in resource-constrained environments, ultimately contributing to better patient survival rates.

Corresponding Author:

Ayodeji Olalekan Salau
Department of Electrical/Electronics and Computer Engineering, Afe Babalola University
Ado-Ekiti, Nigeria
Email: ayodejisalau98@gmail.com

1. INTRODUCTION

Lung cancer remains one of the deadliest cancers worldwide, accounting for approximately 18% of all cancer-related deaths [1]. The World Health Organization (WHO) estimates that by 2030, lung cancer will be responsible for about 17 million deaths globally. Early detection significantly improves outcomes, with survival rates reaching nearly 50% when the disease is diagnosed at an early stage [1]. Chest X-ray imaging is often used as an initial screening tool; however, its limited ability to detect small nodules and lack of cross-sectional imaging reduce its diagnostic effectiveness, making it more suitable for preliminary screening than definitive diagnosis [1], [2]. Consequently, advanced imaging modalities such as MRI, PET, PET/CT, and PET/MRI are frequently employed, each providing distinct benefits and trade-offs in terms of diagnostic accuracy, cost, and clinical utility [3].

Computed tomography (CT) is another imaging modality widely used for lung cancer diagnosis. It employs X-rays and is among the most effective techniques for detecting lung lesions [3]. In recent years, low-dose computed tomography (LDCT) has demonstrated significant improvements in early lung cancer detection [3]. Compared with chest X-ray imaging, conventional CT involves higher radiation exposure, measured in milli-seivert (mSv). However, LDCT performed at 25 mA and 80 kV, with a radiation dose of 22.3 mGy·cm (approximately 0.3 mSv), does not compromise sensitivity for lung cancer detection [4]. The radiation dose associated with LDCT (0.3–0.6 mSv) is substantially lower than that of standard CT, which ranges from 3.5 to 7 mSv [3], [4]. Owing to its high spatial resolution, CT imaging enables reliable detection of small pulmonary nodules. Figure 1 illustrates CT images of a normal lung and a patient with confirmed lung cancer.

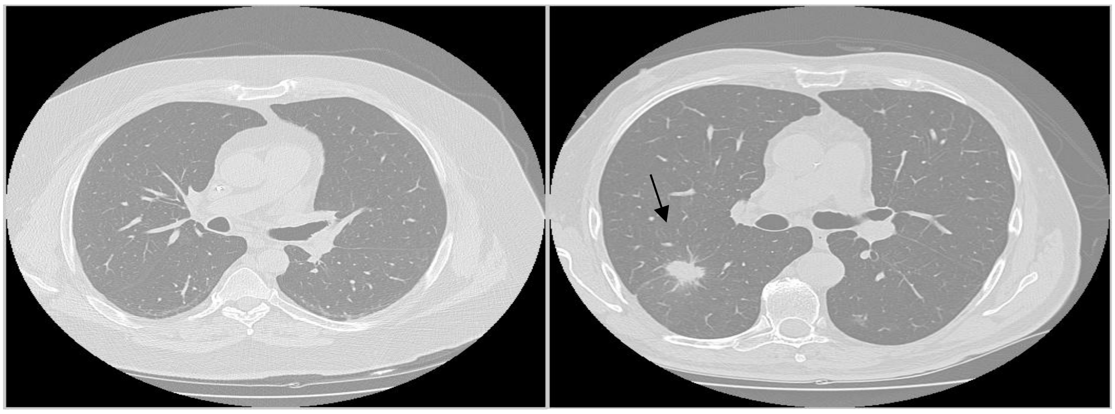

Figure 1. CT image with lung cancer (right) and another without lung cancer (left)

Although CT imaging is highly sensitive, it presents challenges in visually distinguishing between benign and malignant lesions [5]. Consequently, manual interpretation is prone to misdiagnosis, highlighting the need for automated diagnostic systems. Computer-aided detection (CADe) and computer-aided diagnosis (CADx) have therefore emerged as effective approaches for the early detection of lung cancer [1].

Most CADe systems follow a similar pipeline comprising signal acquisition, preprocessing, segmentation, and classification [5]. Extensive research has been conducted on CADe systems to minimize diagnostic errors and reduce the risk of misclassification. In this context, techniques based on integral transforms have demonstrated considerable potential.

The present work proposes a novel approach for lung tumor detection in chest CT images by combining spatially localized integral transforms with convolutional neural network (CNN)-based classification. Various methodologies can be adopted in the development of a CADe system. In this study, three key stages are emphasized: spatial image enhancement, integral transforms, and image classification. Spatial domain enhancement: Image enhancement is a fundamental component of most CADe systems, addressing multiple aspects of image quality, including saturation, sharpness, noise reduction, tonal adjustment, tonal balance, and contrast enhancement [6]–[8]. Among spatial enhancement techniques, power-law (gamma) transformation is widely used and is mathematically expressed in (1):

$$s = cr^{\gamma} \tag{1}$$

where c and γ are positive constants that control image brightness and contrast, respectively; r denotes the input pixel intensity and s represents the transformed intensity for a given grayscale image [8], [9]. Gamma correction can be classified as either global or local [8]. In global gamma correction, a single gamma value (γ) is applied to the entire image [8]. However, applying a global power-law transformation may lead to over-enhancement or under-enhancement in certain regions of the image [8]. Consequently, it is more effective to apply different gamma values to different regions to achieve improved image enhancement. In this context, several adaptive approaches for determining gamma values have been proposed in the literature.

In a previous study by Rahman *et al.* [8], the gamma value was computed based on local image contrast information. Using Chebyshev's criterion, if at least 75% of a distribution lies within 4σ (where σ is the standard deviation) of its mean, the image is classified as having low contrast; otherwise, it is considered to have normal (moderate-to-high) contrast. Accordingly, Rahman *et al.* [8] defined separate formulations for computing the gamma values for low-contrast and moderate-to-high-contrast images, as given in (2) and (3), respectively.

$$\gamma = -log_2\sigma \tag{2}$$

$$\gamma = exp^{[\frac{1-(\mu+\sigma)}{2}]} \tag{3}$$

where, μ and σ are the mean and standard deviations.

As for the brightness, an image is considered bright if the mean value of the pixels $(\mu) > 0.5$ (assuming the image is normalized between 0 and 1). If not, it is considered dark. For an image considered bright, the value of c is assumed unity, and the gamma transform is computed by (1) using c=1. If not, the gamma transform is computed using (4):

$$s = \frac{r^\gamma}{r^\gamma + (1-r^\gamma)\times\mu^\gamma} \tag{4}$$

where μ is the mean of the image.

Another spatial-domain enhancement technique reported in the literature is the successive mean quantization transform (SMQT). SMQT is an image processing method primarily used to enhance images and compress their dynamic range. It operates by recursively partitioning the data into two groups based on their mean values and performing quantization at each iteration [7]. At each stage of the transformation, the data is separated into upper and lower subsets according to the mean, and these subsets are further subdivided in subsequent iterations. The level of detail preserved during the transformation depends on the number of iterations performed. As a result, SMQT quantizes the data while retaining essential structural information, making it particularly suitable for applications such as contrast enhancement, dynamic feature extraction, and dynamic range compression in images [7].

Another spatial-based segmentation approach is the watershed technique. This method interprets an image as a three-dimensional surface, where the third dimension represents pixel intensity, thereby modeling the image as a topographic landscape [9]. However, direct application of the watershed algorithm often leads to over-segmentation due to noise and local irregularities in the image gradient. To address this issue, a marker-based watershed approach is commonly employed to regulate the segmentation process. In this method, markers are defined as connected components within the image, where internal markers correspond to objects of interest and external markers represent the background regions [9].

Integral transform techniques are also widely used in image processing, including the two-dimensional Fourier transform and the two-dimensional Hartley transform. These transforms convert images from the spatial domain into the spatial-frequency (wavenumber) domain, enabling alternative representations that facilitate improved image analysis and processing [9]. Such transformations offer several advantages, including computational efficiency, enhanced signal representation, and improved image sensing and processing. The discrete forms of the 2D Fourier transform and the 2D Hartley transform are presented in (5) and (6), respectively.

$$F(u,v) = \sum_{x=0}^{M-1}\sum_{y=0}^{N-1} f(x,y)\, exp^{-j2\pi(\frac{ux}{M}+\frac{vy}{N})} \tag{5}$$

$$H(u,v) = \sum_{x=0}^{M-1}\sum_{y=0}^{N-1} f(x,y)\,\frac{1}{2} cas\left(\frac{ux}{M}+\frac{vy}{N}\right) \tag{6}$$

where f is the input image and $cas(\theta) = \cos(\theta) + \sin(\theta)$.

Hartley transform is the same as Fourier transform, but it computes the coefficients of the Fourier transform in the real space without involving complex arithmetic. The Fourier and Hartley transforms are known to be adequate for analyzing 2D images, which are stationary in that the images' frequency characteristics do not change spatially. For images that show spatial frequency variation (a good example is medical images), joint space-wave number transforms are already available for a better localized analysis. These include the 2D Gabor transform and the 2D wavelet transform [10], [11].

Image processing, such as filtering of an image, could be done in the space-frequency domain. For example, a log Gabor filtering was used in Ajil and Sreeram [12] for image preprocessing on CT images due to its reduced DC value and extendedness at high frequency. The discrete 2D Gabor transform is given in (7).

$$G(k,l,u,v) = \sum_x \sum_y f(x,y) g(x-k, y-l) exp^{-j2\pi(\frac{ux}{M}+\frac{vy}{N})} \tag{7}$$

where g is a localizing window function allowed to translate in x and y directions.

The Gabor transform has been used in different applications, including image filtering and feature extraction [12]. The main drawback of the Gabor transform is that it uses a fixed-width sliding window. This makes it challenging to effectively track spatial frequency variations in an image in the Gabor domain [13], and the wavelet transform was introduced to circumvent this main drawback of the Gabor transform.

The 2D wavelet transform is a spatially localized transform like the Gabor transform but applies multi-resolution analysis as opposed to the fixed localizing window used in Gabor filters [10]–[14]. The 2D wavelet transform is given by (8):

$$W_\varphi(m,n,s,\tau) = \frac{1}{\sqrt{s[m,n]}} \sum_x \sum_y f(x,y)\, \varphi_s^\tau(m,n)(x-m, y-n) \tag{8}$$

$\varphi_s^\tau[m,n]$ is the scaled and translated version of the wavelet function at the discrete indices m and n, s represents the scale parameter, and τ represents the translation parameter. We have seen many applications of the Wavelet transform reported in various literature. For example, Gabralla *et al.* [15] showed an application of the wavelet transform in the effective filtering of images corrupted specifically by Gaussian and speckle kinds of noise. Wavelet domain image enhancement has also been used for image segmentation and enhancement. According to Khalifa *et al.* [16], the discrete 2D wavelet transform was used to segment MRI brain images using 4 different filter banks: the low pass, high pass horizontal, high pass vertical, and high pass diagonal. Then, using those output images, clustering and segmentation of the original image was carried out using fuzzy C-means (FCM) clustering. The wavelet transform, unlike the Gabor transform, does not have a direct relation with the Fourier transform, and the transform may not be invertible depending on the type of mother wavelet used.

The Stockwell (S) transform is another integral transform used to process an image in the space-frequency domain [17], [18]. The S-transform is essentially a phase correction of the wavelet transform [17]. The S-transform keeps the referenced phase information, while the wavelet transform does not. Compared to wavelets, the S-transform does have a direct relation with the natural complex Fourier transform, which makes it easier to implement and calculate its inverse [17]. The S-transform is designed in such a way that it has better frequency resolution at lower frequencies and better time resolution at higher frequencies [17]. The 2D version of the discrete S transform has been used in different filtering and other image processing applications. The 2D discrete S-transform is given by [18].

$$S(\tau_x, \tau_y, u, v) = \sum_x \sum_y f(x,y) \frac{|uv|}{\sqrt{2\pi k_1 k_2}} exp^{\frac{-(\tau_x - x)^2 u^2}{2k_1^2} \frac{-(\tau_y - y)^2 v^2}{2k_2^2}} exp^{-j2\pi(\frac{ux}{M}+\frac{vy}{N})} \tag{9}$$

where $\frac{|uv|}{\sqrt{2\pi k_1 k_2}} exp^{\frac{-(\tau_x - x)^2 u^2}{2k_1^2} \frac{-(\tau_y - y)^2 v^2}{2k_2^2}}$ represents the window function.

According to Assefa *et al.* [19], the rotation invariant 2D S-transform was proposed for use in the texture analysis of color images, extending the definition of the S-transform from complex (2D) to the quaternion (4D) space. This transform is used later in the current research through the Hartley transformation. The rotation invariant version of the 2D S-transform proposed in Assefa *et al.* [19] is given by (10):

$$S(\tau_x, \tau_y, u, v) = \sum_x \sum_y f(x,y) \frac{u^2+v^2}{2\pi r^2} exp^{-\{(\tau_x - x)^2 + (\tau_y - y)^2\}\frac{(u^2+v^2)}{2r^2}} exp^{-j2\pi(\frac{ux}{M}+\frac{vy}{N})} \tag{10}$$

for some constant r.

Image classification: many works have been proposed in the area of image classification. Specific to lung cancer detection based on CT images, the main aim is to differentiate between benign and malignant. Machine learning is the best way of classification. There are different machine learning categories: supervised, unsupervised, semi-supervised, and reinforcement learning. In most cases the conventional machine learning does not apply to medical images due to the dynamic nature of the images [1], [20], [21].

Deep learning is a supervised learning paradigm that employs multi-layer neural networks for model training. This hierarchical structure enables deep learning models to capture complex image features and relationships, often achieving superior performance compared to conventional machine learning approaches. Commonly used supervised deep learning architectures include CNNs, long short-term memory (LSTM), recurrent neural networks (RNNs), and gated recurrent units (GRUs) [1], [22].

Lee *et al.* [23] demonstrated the application of CNNs for lung nodule segmentation and discussed several deep learning–based segmentation techniques. These include fully convolutional networks (FCNs), which replace fully connected layers with convolutional layers to achieve large receptive fields, enabling segmentation through coarse class score maps generated via feed-forward processing of input images. Another prominent approach is Mask Region-based CNN (Mask R-CNN), which performs object detection while simultaneously producing segmentation masks. SegNet is another semantic, pixel-wise segmentation model that has been widely applied in medical imaging [24].

Among these methods, U-Net has gained significant attention due to its effectiveness and extensive use in medical image segmentation. A summary of related studies employing different classification methods is provided in Table 1. An analysis of the studies summarized in Table 1 reveals that many existing methods depend on large-scale datasets for training and evaluation, requiring substantial computational resources such as high memory capacity and powerful GPUs.

Table 1. Comparison of datasets used, methods, and accuracies for different papers

Author	Purpose	Dataset/no. of image data	Method	Result	Year of publication
Lakshmanaprabu *et al.* [20]	Lung CT-image classification to benign, malignant, and normal	70 images	ODNN classifier with MGSA	Accuracy 94.56%	2018
Cifci [21]	Lung CT-image classification to benign, malignant, and normal	TCIA dataset/ 46,698 images	SegChaNet	Accuracy 98.9%	2022
Hu *et al.* [22]	Lung segmentation	Raw images of hospitals/ 13,000 images	Supervised and unsupervised learning with image erosion and dilation	Accuracy 97.11%	2020
Lee *et al.* [23]	Lung segmentation	LIDC	U-Net	Accuracy 95.02%	2018

In contrast, the current research focuses on developing a computationally efficient and accurate approach that operates with limited resources and smaller training datasets. Accordingly, a CT-based lung cancer detection framework is proposed, which integrates a spatially localized integral transform for feature extraction with a U-Net–based classification model. The approach utilizes images from The Cancer Imaging Archive (TCIA), selected based on their responses to marker-controlled watershed and area filtering techniques. It is important to note that the proposed method is primarily designed to detect lung cancers located in peripheral regions, rather than those situated in central lung areas.

2. METHOD

2.1. Materials used

The proposed system was implemented using an image dataset obtained from TCIA database [25]. CT lung images with the specified characteristics were employed for testing and validation, as summarized in Table 2. The complete lung cancer detection and classification framework was developed using the MATLAB platform, chosen for its extensive built-in functions, ease of rapid prototyping, availability of pre-trained networks, comprehensive documentation, and suitability for academic research. The proposed algorithm was executed on a system equipped with an Intel Core i5 processor operating at 2.5 GHz, 8 GB of RAM, and a Microsoft Windows operating system.

Table 2. Image information

Resolution	Depth	CT-model	Type of compression
512×512	16 bits	Helical mode scan	DICOM

2.2. Procedures

Image pre-processing: after evaluating the dataset images, the histograms of the input images showed no significant noise distribution; therefore, no prior image smoothing was applied. Image selection was performed as the first step. The dataset images were initially chosen based on their suitability for segmentation using marker-controlled watershed and area filtering techniques.

Pre-processing focuses on isolating the lung region exclusively, as most lung malignancies—particularly non-small cell lung cancer—originate in the lung parenchyma. This approach also effectively separates large blood vessels near the central region, thereby improving the accuracy of the final classification.

Subsequently, 81 lung images were selected from the dataset. Marker-controlled watershed segmentation was used to separate relevant structures from the CT images. Through observation and quantitative analysis, the lung region was found to occupy approximately 10–35% of the image area. Based on these limits, an area filter was designed to retain only the lung region.

$$BW(x,y) = Area\{MarkerW[I(x,y)]\} \tag{11}$$

$I(x,y)$ is the input image from the dataset. $Marker\{W\}$ shows the implementation of the marker-controlled watershed algorithm on an image. $Area[\,]$ shows the implementation of area filtering with the mentioned parameters on a marker-controlled watershed segmented image.

Following lung segmentation, the image is cropped and resized. Image cropping comes first, followed by image resizing. The input image has 16-bit depth and 512×512 resolution. This image is transformed into a 4D signal (512×512×512×512) by feature extraction. 137 gigabytes of internal RAM are needed for this (which is unattainable for low resource settings). Therefore, image cropping and scaling are done to make the image size appropriate for processing. Parts of the image that are unsuitable for diagnosis, such as the dark portion of the CT scan, are cropped out. The results of marker-controlled watershed and area filtering are used to determine the cropping. By translating vertically and horizontally from the white pixels, this image (BW(x, y), binary image) gives us both vertical and horizontal cropping dimensions. By applying the acquired dimensions to the original image, it is accomplished automatically. To lessen the impact of aliasing that can happen when scaling the image later, cropping is done first. By cropping an image, its original size would be reduced to about 25% of its original size (to 256×256) without compromising the quality. As a consequence, using image scaling greatly decreased aliasing. Bicubic interpolation of an integrated MATLAB function is used for the resizing. The final image was 120×150 pixels and was normalized between [0,1]. After that, an image picture is subjected to Wiener filter smoothing with a 3×3 window size to eliminate any noise that may have resulted from earlier processes.

$$I'(x,y) = wiener[cropresize(I(x,y))] \tag{12}$$

$$BW'(x,y) = cropresize(BW(x,y)) \tag{13}$$

For *image* $I'(x,y)$ the dimensions for cropping are obtained from *image* $BW(x,y)$. $BW'(x,y)$ is the cropped image of $BW(x,y)$ that will be used later.

Image enhancement*:* at this stage, two techniques of spatial domain image enhancement were implemented on the pre-processed images: SMQT and the adaptive gamma correction, both introduced earlier. The first enhancement was used to create a better contrast image. An 8-level SMQT was used in this regard. Here, the cropped and resized image from the previous stage will be enhanced. Before using the SMQT, the depth of the image will be reduced from 16-bit to an 8-bit image. This will ensure fast computation and efficient memory consumption for the later stage. The SMQT delivers quantization to the pixel intensities of the image. The quantization characterizes the image intensities with finite intensity values. This does ensure the reduction of image information to only specific groups of pixel intensities. This would help for characterizing the image by specific intensity feature, which will later be used in image feature extraction and segmentation. However, the enhancement might introduce some unnecessary intensity values. For example, boundary valued (only slightly greater than the mean) intensities might acquire false intensities. Thus, the brightness-controlled adaptive gamma correction (discussed in the literature) was implemented to reduce this error. This enhancement would correct contrast and brightness as well. The formula for the process is shown in (14):

$$f(x,y) = brigthness\ controlledgamma[SMQT(I'(x,y))] \tag{14}$$

Image feature extraction and segmentation: an integral transform-based approach was implemented to extract useful features. The transform domain gives another perspective on image analysis. There are different integral transform methods, one of which is the Fourier transform. The Fourier transform is a very basic and useful approach that gives only the frequency information of the signal. It has no information concerning the spatial location of frequencies, which makes it difficult to decide between useful edge and noise. As a result, a better technique is a space-frequency approach. Space-frequency integral transform gives both spatial and frequency information with relative resolution for both parameters. There are different space-frequency approaches; short-time Fourier transform (STFT) is one with a constant window size and limited space-frequency resolution. As compared to STFT, wavelet transform can achieve better space-frequency resolution by providing variable window size. However, wavelet transform invertibility depends on the choice of the wavelet. Moreover, no direct relation with Fourier transform makes it difficult to interpret and implement basic operations on the transformed domain. Thus, rotation-invariant spatially localized transform is chosen to better suit the feature extraction. The rotational-invariant integral transform has better invertibility while maintaining a direct relation with the Fourier transform as compared to the wavelet transform. In addition, the rotation invariance nature makes a robust feature extraction that does not vary with rotation motion. Thus, the rotation invariant spatially localized integral transform method was chosen for feature extraction.

Thus, after the image preprocessing and spatial enhancement, the image will be transformed to the space-frequency domain, resulting in a 4-dimensional signal. It is implemented using the Hartley transformation, using even and odd calculations without complex computation as shown in (15). It contains the spatial coordinates and their respective frequency components (τ_x, τ_y, u, v). For a single pixel, there are the row (u) and column (v) frequency components. Then, the power of the transform is calculated as shown in (16):

$$F\left(\tau_x, \tau_y, u, v\right) = \sum_x \sum_y f(x, y)\, \frac{u^2+v^2}{2\pi r^2}\, exp^{-\{(\tau_x - x)^2 + \left(\tau_y - y\right)^2\}\frac{(u^2+v^2)}{2r^2}}\, \frac{1}{2}\, cas(\frac{xu}{M} + \frac{yv}{N}) \quad (15)$$

$$F'(\tau_x, \tau_y, u, v) = F^2(\tau_x, \tau_y, u, v) \quad (16)$$

In (15) calculates the rotation invariant integral transform of the input image $f(x, y)$ resulting in 4-dimension $F\left(\tau_x, \tau_y, u, v\right)$. While (16) calculates the Fourier power of the transformed 4D signal resulting in $F'(\tau_x, \tau_y, u, v)$. After determining the power of the spectrum image, different statistics were tried to fork out the better features. Different statistics (mean, median, standard deviation, and sum) were tested. And the sum responded well. The sum of the power spectrum is implemented by summing up the frequency components and reducing the signal dimension to become 2-dimension. The process is shown in (17):

$$G(\mathrm{x}, \mathrm{y}) = \Sigma_{\mathrm{u}}\ \Sigma_{\mathrm{v}}\ F'(\tau_x, \tau_y, u, v) \quad (17)$$

After calculating the sum of the power spectrum, the result matrix is normalized between [0,1], which is suitable for further calculation. Then, different gamma values were tested on the resulting image, and the 10th root was found adequate with the best response. Then, the resulting image is subtracted from the normalized spatial-enhanced image.

$$\mathrm{G}'(\mathrm{x}, \mathrm{y}) = \mathrm{f}(\mathrm{x}, \mathrm{y}) - \mathrm{G}^{\frac{1}{10}}(\mathrm{x}, \mathrm{y}) \quad (18)$$

Since the tumor has different signatures from the other nodules, this procedure will eliminate pixels that are non-cancerous. Then, the cropped and resized marker-controlled watershed segmented image from the preprocessing is imposed on the original image and smoothed with a 7×7 wiener filter. Finally, the resulting image will be added to $\mathrm{G}'(\mathrm{x}, \mathrm{y})$.The process is shown in (19):

$$\mathrm{G}''(\mathrm{x}, \mathrm{y}) = \mathrm{G}'(\mathrm{x}, \mathrm{y}) + \mathrm{wiener}[\mathrm{BW}'(\mathrm{x}, \mathrm{y}) + \mathrm{I}'(\mathrm{x}, \mathrm{y})] \quad (19)$$

Then, finally, a simple thresholding of the image $\mathrm{G}''(\mathrm{x}, \mathrm{y})$ is done as a result of which the cancer nodule would always yield a constant signature map (green in HSV plot or 0.125-0.29 in double image. This procedure is used to amplify the tumor signature more and make it suitable for the U-net architecture. Then, after, the thresholded image $\mathrm{G}''(\mathrm{x}, \mathrm{y})$ is used for CNN-based classification scheme training together with an annotated binary image (ground truth).

Image classification: for image classification, CNN-based U-NET semantic image segmentation was implemented. The U-NET was chosen since the main aim of U-NET itself is for medical image segmentation, and it can learn from a few images when the images are well-suited for segmentation. The feature extraction and earlier stages of the proposed system can successfully deliver suitable images for the U-NET classification training. In addition, U-NET is simple, easy to train, implements fewer control parameters, absence of intermediate layers makes it an ideal choice for classification. Even though U-NET ++ has better accuracy, the U-NET weakness is filled with the feature extraction scheme of this approach. It is implemented here without any modification. The images from feature extraction and annotation (ground truth) were used for the training. From 81 images, 49 (29 are abnormal) images are used for training and 32 (17 are abnormal) for testing.

Conventionally, the training and testing split ratio is 80:20. In this research, since the target is to minimize the resources used for training, 60% of the data randomly chosen from feature-extracted and annotated images, was used, and the rest for testing. All images are resized to 128×128, which helps to integrate with the U-NET classification. The classification categories are background (0-normal lung) and foreground (1-tumor). An inbuilt MATLAB function, unetLayers, was used to implement U-NET CNN architecture for its simplicity and low resource requirement. The U-NET here implements 46 layers, encoders (for down sampling), and decoders (for up-sampling), drop-out (to avoid overfitting), and pixel classification (to measure the discrepancy between ground truth and predicted).

The cross-entropy loss function is implemented. The encoder contains the convolutional layers followed by rectified linear units (ReLU). The convolutional layer convolves the input lung image and the weight matrix for the extraction of features. The ReLU is an activation function that calculates the maximum value of the result. This will produce a non-linear relation among features. Then, the features go through max pooling for down sampling of the signal. The decoder localizes the features spatially and reconstructs the image. A skip connection is used to link the decoder with the encoder. It contains upsampling, concatenation, and convolution layers with ReLU. The U-NET implemented here does not use pre-trained CNNs. It is implemented by encoders and decoders. However, different hyperparameter combinations have been tried. These hyperparameter combinations are (epochs [200,100,50,10], optimizers [Adam, sgdm], mini batches [2, 4, 10] and encoder depth [3, 5]). The U-NET implementation using the SGD optimizer, 50 epochs, 4 mini-batch sizes, and an initial learning rate of 1e-3 yielded the best result. After classification, simple morphological image cleaning was done through image opening by implementing a disk structuring element of size 1.

Testing and validation: there are two ways of testing the algorithm, based on qualitative output and measurable (quantitative) parameters. The quantitative parameters are measured in terms of true positive (TP), true negative (TN), false positive (FP), and false negative (FN). Since the main aim of the research is to differentiate between the normal nodules of the lung (blood vessels and normal spots) from tumors. In this regard, TP means the white spot (nodule) in the CT images of the lung classified to be a tumor as compared with the ground truth. And TN means a nodule in the CT image of the lung classified to be non-tumor/normal as compared to the ground truth. FP is a nodule wrongly classified as a tumor, and FN tumor wrongly classified as normal. Thus, while testing, the total number of nodules is counted. Then, the respective values for the TN, TP, FP, and FN are counted accordingly. Based on their count result, the accuracy, specificity, and sensitivity are calculated using (20)–(23). Based on these assumptions, the following parameters are calculated.

$$Accuracy = \frac{TP+TN}{TP+TN+FP+FN} \tag{20}$$

$$Sensitivity = \frac{FP}{TP+FN} \tag{21}$$

$$Specificity = \frac{TN}{TN+FP} \tag{22}$$

In addition, the F1-score has also been used.

$$F1-score = \frac{2*TP}{2*TP+FP+FN} \tag{23}$$

On the other hand, the segmentation and classification accuracy parameters are the intersection over union (IoU) and dice similarity coefficient (DSC) calculated using (24) and (25). I_A and I_B represent the classified image and the ground truth image, respectively.

$$IOU = \frac{|I_A \cap I_B|}{|I_A \cup I_B|} \tag{24}$$

$$DSC = \frac{2*|I_A \cap I_B|}{|I_A|+|I_B|} \tag{25}$$

Figure 2 illustrates the overall workflow of the proposed method. The process begins with an input CT image of size 512×512 pixels. Following preprocessing, the image is enhanced to improve visual quality and feature visibility. The enhanced image is then subjected to the feature extraction stage, and the resulting features are subsequently used for classification. Representative outputs from each processing stage are shown sequentially up to the final classification result.

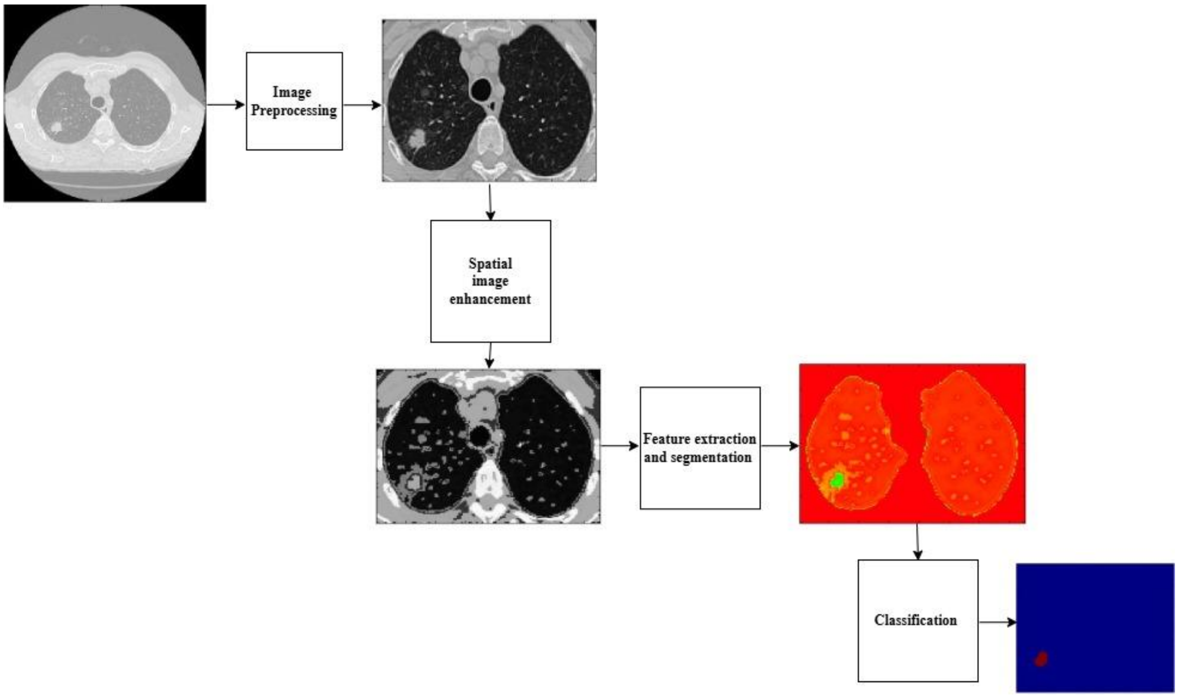

Figure 2. Summary of the methodology

3. RESULTS AND DISCUSSION

Selected qualitative and quantitative results have been presented here to demonstrate the effectiveness of the proposed cancer detection scheme, accompanied by discussions.

3.1. Qualitative results

Results from image pre-processing: the input image is a DICOM image with 512×512 resolution and 16-bit depth, as was covered earlier in the process. Making this image suitable for the process to follow and for feature extraction is, thus, the primary goal of the preprocessing. It entails scaling and cropping the image. Figure 3 shows the results from the pre-processing of the DICOM images. The input image (to the left) is displayed in Figure 3(a). Figure 3(b) is produced by applying marker-controlled watershed and area filtering to the input image. Only the lung portion is segmented in the binary image. Since most cancer nodules develop in the periphery of the lung parenchyma, segmenting the lung is crucial. In the technique, we referred to this image as *image-BW*. Using this image, automated cropping dimensions are calculated by translating vertically and horizontally from the lung edges. Using these dimensions, the original image is cropped and then resized to a suitable resolution (120×150). After that, it is filtered with a 3×3 Wiener filter to smooth out any noise that could have occurred in the process. The image is shown in Figure 3(c). This is the image labeled *image-I*' in the methodology section. Evaluating *image-I'*, it can be seen that the cropped-out part of the image is unnecessary for the diagnosis. Moreover, the cropping and resizing did not affect the details inside the lung parenchyma. As a result, it reasonably suits the process to follow and feature extraction.

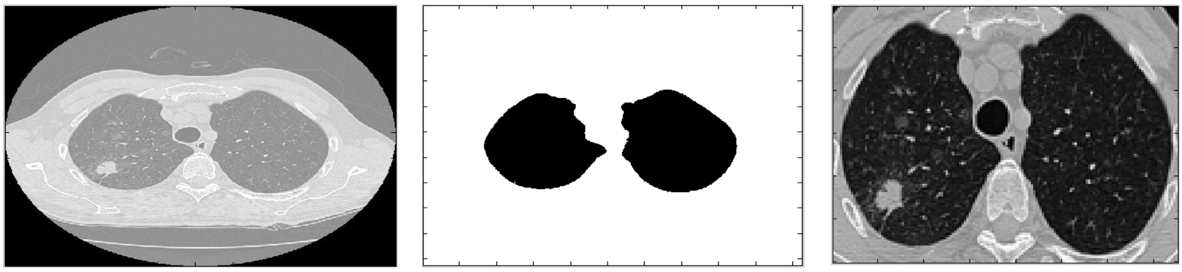

(a) (b) (c)

Figure 3. Results from the pre-processing of the DICOM images; (a) original DICOM image, (b) correctly segmented lung part by marker-controlled watershed and area filtering, and (c) cropped, resized, and filtered image

Results from spatial image enhancement*:* the image enhancement makes the image attain better contrast. Figure 4 shows the results from the spatial image enhancement. Two techniques were implemented for spatial image enhancement: the SMQT and brightness-controlled gamma correction. The input to this procedure is the preprocessed image (*image-I'*), shown in the Figure 4(a). However, the image in Figure 4(b) looks darker. Hence, brightness-controlled gamma correction is used to enhance this. This helps to have better contrast with preserved intensity quantization and reduced darkness. In addition, the brightness-controlled gamma correction will smooth out artificially created intensities at the boundary of each mean calculation. The image result is shown in Figure 4(c). The histogram plot of the input image is shown in Figure 4(d). The histogram plot is continuous and skewed to the bright intensities. The SMQT is used to enhance the contrast and quantize the pixels, as it is shown in the histogram plot Figure 4(e) and the histogram after the application of brightness-controlled gamma correction is shown in Figure 4(f). The spatial enhancement made the nodules inside the lung parenchyma have specified intensities (slightly different in signature for abnormal and normal nodules), making them suitable for feature extraction. Thus, this image is used for feature extraction.

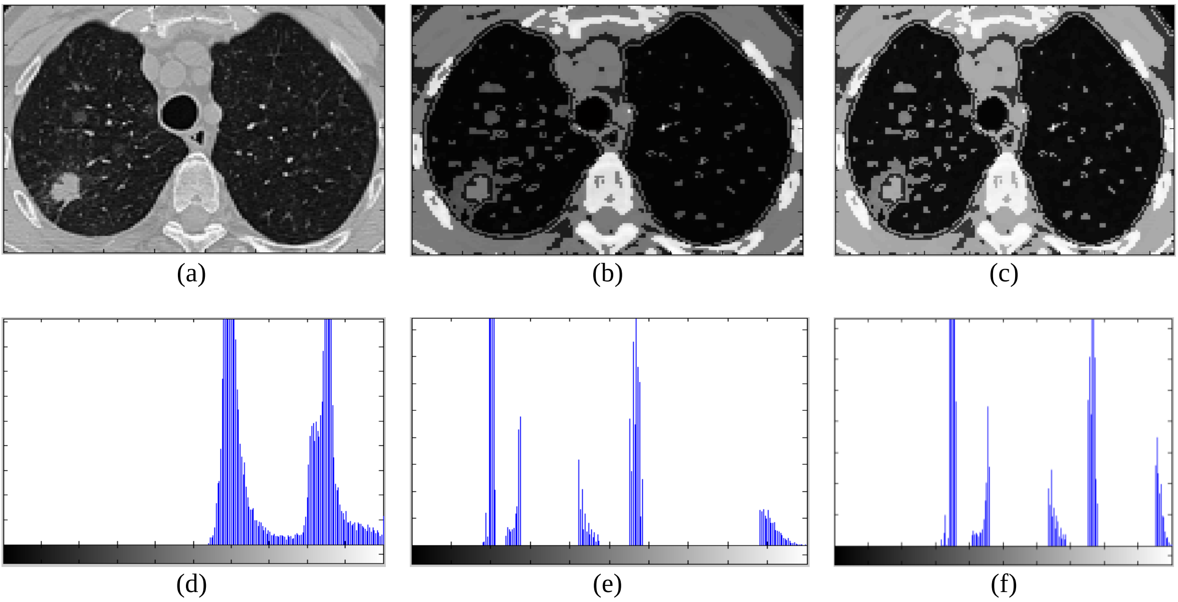

Figure 4. Spatial image enhancement results; (a) input CT image, (b) SMQT-enhanced image, (c) brightness-controlled gamma-corrected image, (d) intensity histogram of the input image, (e) intensity histogram after SMQT enhancement, and (f) intensity histogram after brightness-controlled gamma correction

Results from image feature extraction and segmentation: the enhanced image will be used for extracting important features. Figure 5 shows the results of feature extraction and segmentation. Figure 5(a) shows the input image (*image-f(x,y)*) to the feature extraction and segmentation scheme. This image will be transformed to the space-frequency domain using spatially localized rotational invariant integral transform, resulting in a 4-dimensional signal. Then, the sum of the frequency components of the local power of the 4-dimensional signal is calculated, yielding 2-dimensional features (*image-G(x,y)*). This is shown in Figure 5(b). From the figure, it can be noticed that the tumor indicated by red contour has different signatures for the input image, see Figure 5(a) and the 2-dimensional feature image, see Figure 5(b). Then, the normalized 2-dimensional feature image is gamma corrected with gamma value of 0.1 and subtracted from input image (*image-f(x,y)*). The HSV-pseudo coloring color map of this operation is shown in Figure 5(c) (*image-G'(x,y)*). This image showed the different color signature for malignant (dark-blue/blue) and non-cancerous (sky-blue) nodule. Then Figure 5(d) is the 7×7 wiener filter smoothed sum of the cropped and resized marker-controlled watershed and area filtered image (*image-BW'(x,y)*), and cropped and resized input image (*image-I'(x,y)*). The result showed a little signature for the tumor suppressing other nodules, as shown by the red contour. This image is then added to the *image-G'(x,y*), resulting in Figure 5(e) (image-*G"(x,y)*). The HSV-pseudocolor image showed a green signature for the tumor, differentiating it from other nodules. Finally, a simple thresholding is done to generate Figure 5(f). However, the edges of the lung have the same kind of signature as the tumor, which may lead to a false positive. Thus, the feature extraction and segmentation need further classification. The image classification scheme is trained and tested using the output of the feature extraction and segmentation.

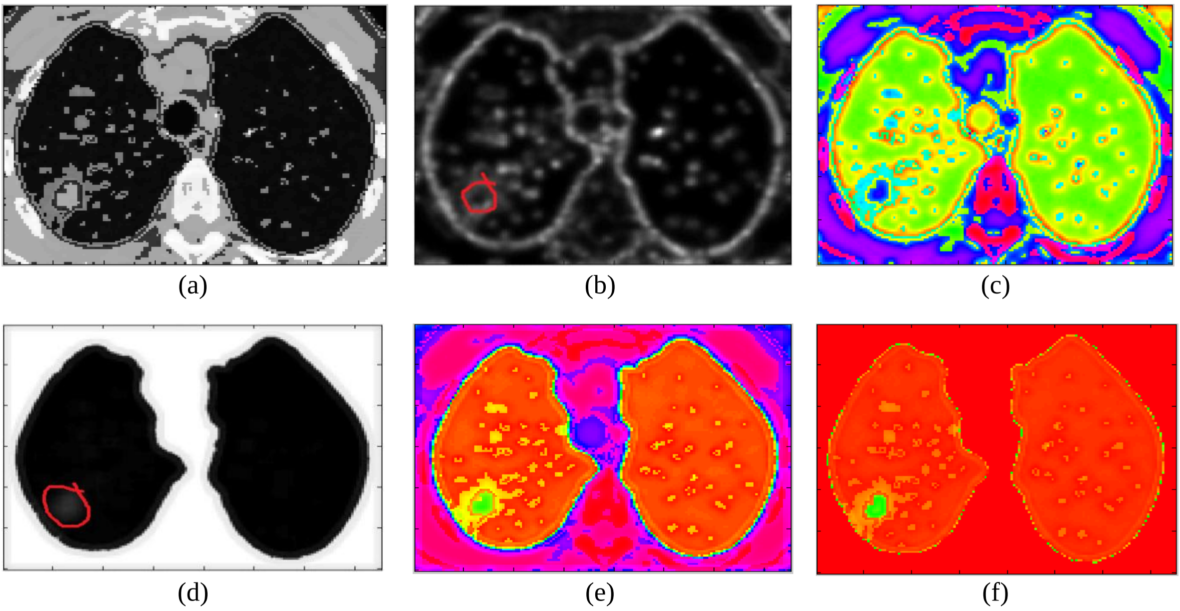

Figure 5. Feature extraction and segmentation results; (a) input CT image, (b) rotationally invariant power spectrum map, (c) difference image, (d) marker-controlled watershed and area-filtered segmentation, (e) combined feature and segmentated image, and (f) final thresholded segmentation

3.2. Result of image classification

Figure 6 illustrates the output of the image classification stage using the U-NET architecture. As described in the methodology, three encoder blocks were implemented using MATLAB's built-in unetLayers function. The U-NET was trained using images obtained from the feature extraction and segmentation stage rather than the original CT images. These images were resized from 120×150 to 128×128 to match the network input requirements. Different numbers of training epochs were evaluated, and 50 epochs produced the best classification performance. From the total of 81 images, 49 were randomly selected for training and 32 for testing. As shown in Figure 6, the classification results consist of two classes: foreground (tumor) and background. This classification stage is essential for reducing false positives, particularly those occurring along the edges of the lung parenchyma and those introduced by the inherent characteristics of CT images and the applied processing scheme. To further ensure that no noise artifacts were introduced, a morphological opening operation using a disk-shaped structuring element was applied. The resulting JET color map reveals well-defined and compact cancer signatures, demonstrating the effectiveness of the proposed detection scheme. Figure 6 also presents the overall U-NET workflow, showing the input image and the corresponding classification output. In cases where no tumor is present, the classification stage correctly suppresses false detections, yielding a final output with no tumor regions.

The image is encoded and down-sampled on the left side of the U-NET architecture, and the right side shows decoding and upsampling procedures. The final result is shown in a JET-color map, showing the tumor classified from the background.

3.3. Quantitative results

In this section, the qualitative results are presented in a comparative manner. The discussion is organized into two subsections: training and testing. The aim is to highlight the importance of feature extraction for classification performance, as well as the role of classification in validating the extracted features. A total of 81 images were used for both training and testing.

3.3.1. Training

The U-NET classifier was trained using 49 images. Various training configurations were evaluated, including different numbers of epochs (10, 50, 100, and 200) and different input image types. These input types comprised feature-extracted and segmented images, as well as the original CT images without enhancement or feature extraction.

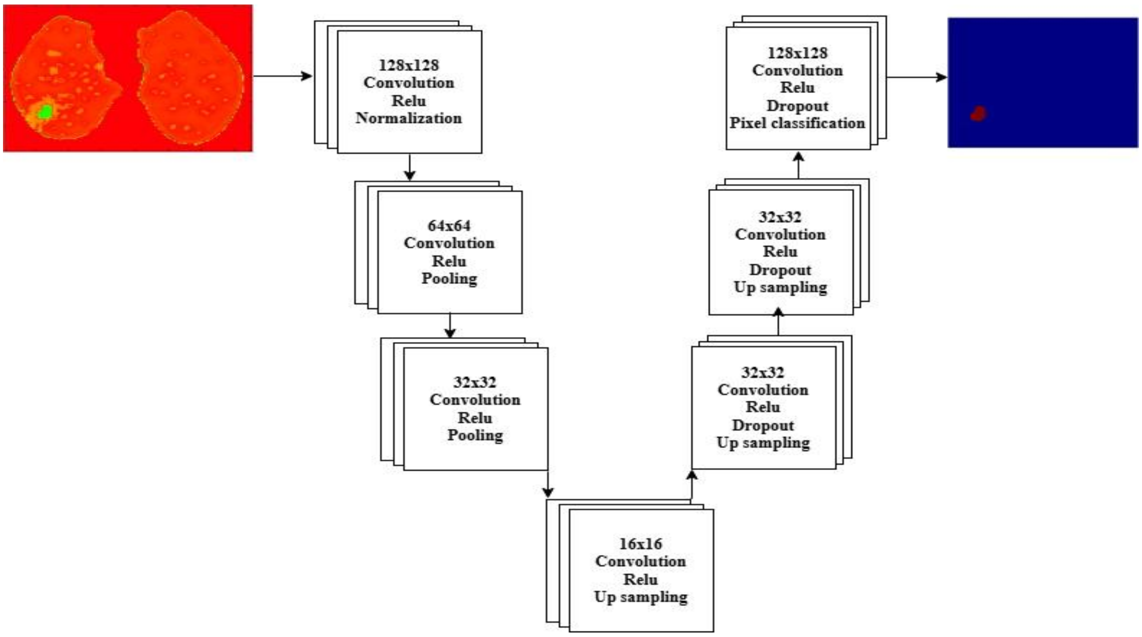

Figure 6. Demonstration of the U-Net Classifier, the input image to the U-NET classifier is shown in HSV color map while the final result is shown in a JET-color map showing a red tumor signature with surrounding blue normal background

Other parameters were kept common for all the tests: *minibatch size-4*, *optimization-sgdm*, *initial learn rate*-1e$^{-3,}$ and encoder depth-*3* and *46-layers*. The U-NET trained with the original image and the U-NET trained with the feature extracted-segmented image were compared. The training performance was evaluated by comparing accuracy, loss (using cross-entropy as the loss function), training time, IoU, and DSC. Among the different epoch settings, 50 epochs demonstrated superior overall performance. At this setting, the model achieved a final training accuracy of 99.93% with a total training time of 137 minutes using the specified computational resources. In contrast, training the U-NET using the original images required more than 15 hours. Accordingly, a brief comparison was conducted between training with feature-extracted segmented images and training with the original images.

Figure 7 presents a comparison of training accuracy for the feature-extracted segmented images and the original images over 50 epochs. Although the training accuracies appear comparable, the U-NET trained on original images fails to generalize effectively when applied to the testing set. Training accuracy was computed with respect to binary ground-truth masks from the dataset. The final training accuracies for the original-image-trained and feature-extracted segmented-image-trained models were 99.93% and 99.75%, respectively.

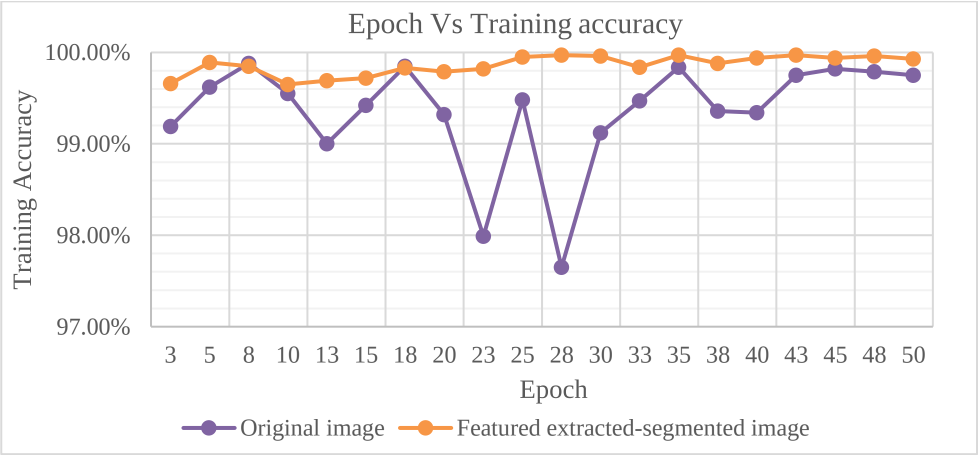

Figure 7. Training accuracy comparison for 50 epochs of the feature extracted-segmented image, and the original image

Figure 8 compares the corresponding training losses for both approaches. It is evident that training on original images results in significantly higher loss values compared to training on feature-extracted segmented images. When Figures 7 and 8 are jointly considered, training with feature-extracted segmented images yields better overall performance, characterized by higher effective accuracy and lower loss. Although the numerical training accuracies are similar, the segmentation efficiency of the U-NET trained on feature-extracted images is markedly superior.

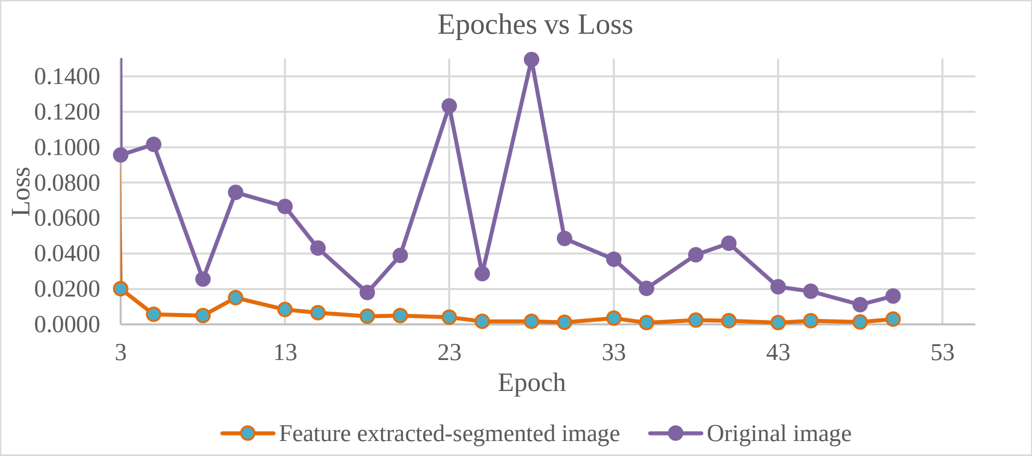

Figure 8. Training loss for both schemes of training

Table 3 summarizes the final-iteration training accuracy, loss, training duration, IoU, and DSC for both training schemes. The results clearly indicate that the feature-extracted segmented image approach outperforms the original image-based training across all evaluated metrics. Consequently, this scheme is adopted for subsequent testing and comparative analysis to demonstrate the effectiveness of the proposed U-NET classification framework.

Table 3. Result signifying the use of feature extraction and segmentation

Epoch size 50	Training accuracy (%)	Loss	Time it takes	IoU	DSC
Original image trained	99.75	0.016	~930 min	0.011	0.021
Featured extracted-segmented image	99.93	0.003	~137 min	0.873	0.929

3.3.2. Testing

To compute the system’s accuracy, specificity, and sensitivity, lung nodules in the original CT images were manually counted. After segmentation or classification, only nodules exhibiting specific signature maps indicative of tumors were considered in the counting process. In the qualitative results, abnormalities in the feature extraction and segmentation outputs are represented in green using the HSV pseudo-colormap, while all other colors indicate normal tissue.

In contrast, for the classification results, abnormalities are represented in white in the grayscale colormap. Based on these criteria, nodules were manually counted to determine correct and incorrect classifications. This manual evaluation was adopted because the primary objective of the study is to differentiate abnormal nodules and detect lung cancer. A total of 32 images, randomly selected from the 81-image dataset, were used for testing. The test set comprised both normal images and abnormal images containing tumors. Nodules were categorized as normal (N) or abnormal (AbN) according to the dataset’s ground truth, which served as the gold standard. Using this reference, true positives (TP), false positives (FP), true negatives (TN), and false negatives (FN) were computed for two cases: feature extraction and segmentation without classification, and feature extraction and segmentation followed by classification.

These results are summarized in Table 4. As shown in Table 4, the numbers of TP, TN, and FN are relatively similar for both approaches. However, a significant reduction in FP is observed when classification is applied. The higher FP count in the absence of classification leads to a lower specificity. Moreover, false positives occurring at the lung boundaries adversely affected the segmentation performance, resulting in lower IoU and DSC values. The incorporation of the classification stage effectively mitigates these issues, substantially improving specificity as well as IoU and DSC performance.

Table 4. TP, FP, TN, and FN values computed using the proposed algorithm using the available gold standard information

Images	Gold standard			With classification				Without classification			
	Total	AbN	N	FP	FN	TP	TN	FP	FN	TP	TN
Im-1	27	1	26	0	0	1	26	0	0	1	26
Im-2	26	1	25	0	0	1	25	0	0	1	25
Im-3	27	1	26	0	0	1	26	0	0	1	26
Im-4	12	0	12	0	0	0	12	0	0	0	12
Im-5	14	0	14	0	0	0	14	1	0	0	13
Im-6	9	0	9	0	0	0	9	1	0	0	9
Im-7	9	1	8	0	1	0	8	0	0	0	8
Im-8	10	1	9	0	0	1	9	0	0	1	9
Im-9	22	0	22	0	0	1	22	0	0	1	22
Im-10	11	0	11	0	0	1	11	0	0	1	11
Im-11	19	1	18	1	0	1	17	2	0	1	16
Im-12	13	0	13	0	0	0	13	0	0	0	13
Im-13	14	1	13	0	0	1	13	0	0	1	13
Im-14	10	0	10	1	0	0	8	2	0	0	7
Im-15	11	1	10	0	0	1	10	1	0	1	9
Im-16	11	1	10	0	1	0	10	0	1	0	10
Im-17	13	1	12	0	0	1	12	2	0	1	10
Im-18	25	0	25	0	0	0	25	0	0	0	25
Im-19	21	0	21	0	0	0	21	0	0	0	21
Im-20	24	1	23	0	0	1	23	0	0	1	23
Im-21	22	1	21	0	0	1	21	0	0	1	21
Im-22	12	0	12	0	0	0	12	0	0	0	12
Im-23	12	0	12	0	0	0	12	0	0	0	12
Im-24	19	0	19	0	0	0	19	0	0	0	19
Im-25	12	1	11	0	1	0	11	0	1	0	11
Im-26	22	1	21	0	0	1	21	0	0	1	21
Im-27	25	0	25	0	0	0	25	5	0	0	20
Im-28	21	0	21	0	0	0	21	5	0	0	16
Im-29	33	1	32	0	0	1	32	0	0	1	32
Im-30	25	0	25	0	0	0	25	4	0	0	21
Im-31	33	1	32	0	0	1	32	1	0	1	31
Im-32	23	1	22	0	0	1	22	1	0	1	21
Total nodules	587	17	570	2	3	16	567	25	2	16	545

Accordingly, sensitivity, specificity, and overall accuracy values are computed based on the formula given earlier in this document. These parameters are calculated for both cases (feature extraction and segmentation without classification, and feature extraction and segmentation with classification) [26]-[28]. It can be seen from the Table 4 that the classification significantly reduces the false positives inside the lung parenchyma as well as the false positives at the edges of the lung. The test was done ignoring the edges of the lung false positive for feature extracted images [29]. Table 5 illustrates the comparison between feature extraction with and without classification.

Table 5. Comparison between with and without U-net

	Accuracy (%)	Sensitivity (%)	Specificity (%)	IoU	DSC
Without classification	95.50	88.88	39.02	0.072	0.126
With classification	99.32	84.21	88.88	0.87	0.93

The computational efficiency of the proposed algorithm has also been checked. Accordingly, it takes an average of 200.41 seconds for the entire algorithm to run (on a MATLAB platform), starting from loading a given CT lung image until a final classification result is found. The time of computation is reasonably low compared to other, more complicated methods reported in the literature. Table 6 shows the comparison of the proposed system with other literature. It can be observed that the proposed system has accomplished excellent results with limited data and computational resources [30].

Table 6. Comparison of proposed system with other studies

Author	Datasets	Method	Precision/ sensitivity	IoU	F1-score	Accuracy	Dice
Shuvo and Mamun [27]	LUNA16 6801 images	Yolov5 model for lung classification	76%	-	-	-	-
Sun *et al*. [28]	LUNA16 36,317 images	Swim-transform for lung classification	-	-	-	82.3%	-
Wu *et al*. [29]	AHMU-LC 9265 images	RAD-UNET for lung classification	**94.23%**	86.55 %	93.12%	-	-
Lakshmanaprabu *et al*. [20]	70 images	ODNN and modified gravitational search for lung classification	-	-	-	94.56%	-
Cifci [21]	TCIA 44,848 images	SegChaNet without CAM for lung classification	92.15%	-	**96.89%**	96.81%	**93.7%**
Proposed	TCIA 81 images	Integral transformed-based feature extraction and U-NET classification of lung	84.21%	**87.3%**	86.49%	**99.32%**	92.9%

4. CONCLUSION

The primary objective of this study was to develop a robust, simple, and accurate method for lung cancer detection. The proposed approach was implemented on CT lung images obtained from the TCIA dataset, specifically focusing on peripherally located lung cancers. A comprehensive review of existing lung image analysis techniques was conducted to understand current methodologies and identify gaps. Comparative analyses were performed between results from the literature and the proposed method.

The findings demonstrate that improved accuracy, robustness, and efficiency can be achieved even with limited training data and minimal computational resources, provided that effective feature extraction is combined with a CNN-based classification framework. The proposed method achieved an overall classification accuracy of 99.32%, with a precision of 84.21%, F1-score of 86.49%, IoU of 87.3%, DSC of 92.9%, and specificity of 88.88%. These results highlight the efficacy of integrating spatially localized integral transforms with U-NET CNN architectures for enhanced feature extraction and classification of CT lung images. This research underscores the significant role of integral transforms in medical image analysis, particularly for the segmentation and classification of lung cancer. The combination of the 2D spatially localized integral transform and U-Net proved to be a practical and effective approach for accurate lung cancer detection.

For future work, it is recommended to expand the model to classify all types of lung cancer. Additionally, efforts should be made to further improve the precision, F1-score, and segmentation metrics (IoU and DSC). Incorporating raw clinical data from hospitals and clinical trials is also essential to enhance the model's applicability in real-world scenarios, such as predicting related gene proteins in cancer development.

FUNDING INFORMATION

No funding was received to assist with the preparation of this manuscript.

AUTHOR CONTRIBUTIONS STATEMENT

This journal uses the Contributor Roles Taxonomy (CRediT) to recognize individual author contributions, reduce authorship disputes, and facilitate collaboration.

Name of Author	C	M	So	Va	Fo	I	R	D	O	E	Vi	Su	P	Fu
Abel Belay Wossene	✓	✓			✓	✓			✓	✓	✓			
Dawit Assefa		✓	✓		✓	✓			✓	✓				
Ayodeji Olalekan Salau		✓		✓		✓	✓	✓		✓				
Sepiribo Lucky Braide	✓	✓			✓	✓				✓	✓			
Aitizaz Ali	✓	✓		✓	✓	✓				✓				
Ting Tin Tin	✓	✓			✓	✓				✓				

C : **C**onceptualization
M : **M**ethodology
So : **So**ftware
Va : **Va**lidation
Fo : **Fo**rmal analysis
I : **I**nvestigation
R : **R**esources
D : **D**ata Curation
O : Writing - **O**riginal Draft
E : Writing - Review & **E**diting
Vi : **Vi**sualization
Su : **Su**pervision
P : **P**roject administration
Fu : **Fu**nding acquisition

CONFLICT OF INTEREST STATEMENT

The authors declare that they have no conflict of interest.

DATA AVAILABILITY

The datasets generated during and/or analyzed during the current study are not publicly available but are available from the corresponding author on reasonable request.

REFERENCES

[1] M. A. Thanoon, M. A. Zulkifley, M. A. A. M. Zainuri, and S. R. Abdani, "A Review of Deep Learning Techniques for Lung Cancer Screening and Diagnosis Based on CT Images," *Diagnostics*, vol. 13, no. 16, pp. 1-27, 2023, doi: 10.3390/diagnostics13162617.

[2] A. O. Salau, M. R. Pooja, N. F. Hasani, and S. L. Braide, "Model Based Risk Assessment to Evaluate Lung Functionality for Early Prognosis of Asthma Using Neural Network Approach," *Mathematical Modelling of Engineering Problems*, vol. 9, no. 4, pp. 1053–1060, Aug. 2022, doi: 10.18280/mmep.090423.

[3] B. Philip *et al.*, "Current investigative modalities for detecting and staging lung cancers: a comprehensive summary," *Indian Journal of Thoracic and Cardiovascular Surgery*, vol. 39, no. 1, pp. 42–52, 2023, doi: 10.1007/s12055-022-01430-2.

[4] A. Christie *et al.*, "Lung cancer screening: Evaluation of radiologists and different computer-assisted detection software (CAD) as first and second readers for lung nodule detection at different CT dose levels," *European Socieaty of Raiology (Conference)*, 2013, doi: 10.1594/ecr2013/C-2614.

[5] M. Firmino, A. H. Morais, R. M. Mendoça, M. R. Dantas, H. R. Hekis, and R. Valentim, "Computer-aided detection system for lung cancer in computed tomography scans: Review and future prospects," *BioMedical Engineering Online*, vol. 13, p. 41, 2014, doi: 10.1186/1475-925X-13-41.

[6] J. Ma, C. Zou, and X. Jin, "An improved image enhancement algorithm," *Wuhan University Journal of Natural Sciences*, vol. 22, no. 1, pp. 85–92, 2017, doi: 10.1007/s11859-017-1221-x.

[7] M. Nilsson, M. Dahl, and I. Claesson, "The Successive Mean Quantization Transform," in *ICASSP, IEEE International Conference on Acoustics, Speech and Signal Processing - Proceedings*, 2005, doi: 10.1109/ICASSP.2005.1416037.

[8] S. Rahman, M. M. Rahman, M. Abdullah-Al-Wadud, G. D. Al-Quaderi, and M. Shoyaib, "An adaptive gamma correction for image enhancement," *Eurasip Journal on Image and Video Processing*, vol. 2016, no. 1, p. 35, 2016, doi: 10.1186/s13640-016-0138-1.

[9] R. C. Gonzalez and R. E. Woods, *Digital image processing*, 4th ed. New York, NY, USA: Pearson Education International, 2018, doi: 10.1007/978-94-009-7163-9_6.

[10] R. Carmona, W. L. Hwang, and B. Torrésani, *Practical Time-Frequency Analysis*. San Diego, CA, USA: Academic Press, 1998.

[11] R. N. Braceqwell, *The Fast Fourier Transform and its Applications*, 3rd ed. New York, NY, USA: McGraw-Hill, 2000, doi: 10.1109/TE.1969.4320436.

[12] M. V. Ajil and S. Sreeram, "Lung Cancer Detection from CT Image using Image Processing Techniques," *International Journal of Advance Research in Computer Science and Management Studies*, vol. 3, no. 5, pp. 249–254, 2015.

[13] T. Barbu, "Gabor filter-based face recognition technique," in *Proceedings of the Romanian Academy Series A - Mathematics Physics Technical Sciences Information Science*, 2010, pp. 277–283.

[14] R. Polikar, "The Engineer's Ultimate Guide to Wavelet Analysis: The Wavelet Tutorial," Rowan University, College of Engineering Web Servers. [Online]. Available: https://cseweb.ucsd.edu/~baden/Doc/wavelets/polikar_wavelets.pdf.

[15] L. Gabralla, H. Mahersia, and Z. Marwan, "Denoising CT Images using Tavelet transform," *International Journal of Advanced Computer Science and Applications*, vol. 6, no. 5, pp. 125–129, 2015.

[16] I. Khalifa, A. Youssif, and H. Youssry, "MRI Brain Image Segmentation based on Wavelet and FCM Algorithm," *International Journal of Computer Applications*, vol. 47, no. 16, pp. 32–39, 2012, doi: 10.5120/7275-0446.

[17] R. G. Stockwell, L. Mansinha, and R. P. Lowe, "Localization of the complex spectrum: The S transform," *IEEE Transactions on Signal Processing*, vol. 44, no. 4, pp. 998–1001, 1996, doi: 10.1109/78.492555.

[18] D. Assefa, L. Mansinha, K. F. Tiampo, H. Rasmussen, and K. Abdella, "The trinion Fourier transform of color images," *Signal Processing*, vol. 91, no. 8, pp. 1887–1900, 2011, doi: 10.1016/j.sigpro.2011.02.011.

[19] D. Assefa, L. Mansinha, K. F. Tiampo, H. Rasmussen, and K. Abdella, "Local quaternion Fourier transform and color image texture analysis," *Signal Processing*, vol. 90, no. 6, pp. 1825–1835, 2010, doi: 10.1016/j.sigpro.2009.11.031.

[20] S. K. Lakshmanaprabu, S. N. Mohanty, K. Shankar, N. Arunkumar, and G. Ramirez, "Optimal deep learning model for classification of lung cancer on CT images," *Future Generation Computer Systems*, vol. 92, pp. 374–382, 2019, doi: 10.1016/j.future.2018.10.009.

[21] M. A. Cifci, "SegChaNet: A Novel Model for Lung Cancer Segmentation in CT Scans," *Applied Bionics and Biomechanics*, vol. 2022, 2022, doi: 10.1155/2022/1139587.

[22] Q. Hu *et al.*, "An effective approach for CT lung segmentation using mask region-based convolutional neural networks," *Artificial Intelligence in Medicine*, vol. 103, 2020, doi: 10.1016/j.artmed.2020.101792.

[23] S. M. Lee *et al.*, "Deep Learning Applications in Chest Radiography and Computed Tomography," *Journal of Thoracic Imaging*, vol. 34, no. 2, pp. 75–85, 2019, doi: 10.1097/RTI.0000000000000387.

[24] B. A. Skourt, A. El Hassani, and A. Majda, "Lung CT image segmentation using deep neural networks," *Procedia Computer Science*, vol. 127, pp. 109–113, 2018, doi: 10.1016/j.procs.2018.01.104.

[25] B. Zhao, L. H. Schwartz, M. G. Kris, and G. J. Riely, "RIDER Lung CT," *The Cancer Imaging Archive*, pp. 5–6, 2015, doi: 10.7937/K9/TCIA.2015.U1X8A5NR.

[26] The MathWorks Inc., "Marker-Controlled Watershed Segmentation - MATLAB & Simulink Example," *© 1994-2014*, [Online]. Available: http://www.mathworks.com/help/images/examples/marker-controlled-watershed-segmentation.html#zmw57dd0e3422.

[27] S. B. Shuvo and T. B. Mamun, "An automated end-to-end deep learning-based framework for lung cancer diagnosis by detecting and classifying the lung nodules," *arXiv*, pp. 1–7, 2023, doi: 10.48550/arXiv.2305.00046.

[28] R. Sun, Y. Pang, and W. Li, "Efficient Lung Cancer Image Classification and Segmentation Algorithm Based on an Improved Swin Transformer," *Electronics*, vol. 12, no. 4, p. 1024, 2023, doi: 10.3390/electronics12041024.

[29] Z. Wu, X. Li, and J. Zuo, “RAD-UNet: Research on an improved lung nodule semantic segmentation algorithm based on deep learning,” *Frontiers in Oncology*, vol. 13, 2023, doi: 10.3389/fonc.2023.1084096.

[30] S. I. Shelash *et al.*, “lncRNAs’p potential roles in the pathogenesis of cancer via interacting with signaling pathways; special focus on lncRNA-mediated signaling dysregulation in lung cancer,” *Medical Oncology*, vol. 41, no. 12, 2024, doi: 10.1007/s12032-024-02536-w.

BIOGRAPHIES OF AUTHORS

Abel Belay Wossene received B.Sc. in Electrical and Computer Engineering from Hawassa University in 2013. He got his M.Sc. in Biomedical Engineering from Addis Ababa university in 2018. He is now working at Hawassa University as a lecturer in the Department of Biomedical Engineering, under the institute of technology. He is interested on image processing, biomedical instrumentation and artificial intelligence in healthcare researches. He can be contacted at email: abelbelay98@gmail.com.

Dr. Dawit Assefa received the B.Sc. degree in Mathematics (minor in Physics) from Addis Ababa University (AAU), Addis Ababa, Ethiopia. He received the M.Sc. degree in Mathematics in the Applications of Modeling in the Natural and Social Sciences Graduate Program from Trent University, Peterborough, Ontario, Canada and the Ph.D. degree in Applied Mathematics (Scientific Computing) from the UWO, London, Ontario, Canada. During his stay as a research associate in the Radiation Physics Department, Radiation Medicine Program at Princess Margaret Hospital, UHN - University Health Network (Toronto, Ontario, Canada), he was able to establish single as well as multi- parametric MR image feature based algorithms for use in tissue classification, segmentation and also response quantification of patients treated for high grade brain cancers. He was also part of the UHN Biphotonics Program as a Research Associate at the Ontario Cancer Institute (OCI), Toronto, Ontario, Canada. He is currently Assistant Professor at the School of Biomedical Engineering, College of Technology and Built Environment, Addis Ababa University, Addis Ababa, Ethiopia. His major research interests include medical signal and image analysis, color image processing, scientific computing, AI, bioinformatics and operation research (optimization). Most recently, his collaborative research efforts involve translationally-driven imaging research that exploits advanced mathematical and image analysis assets for applications in preclinical and clinical biomedicine research. He can be contacted at email: dawit.assefa@aau.edu.et.

Dr. Ayodeji Olalekan Salau received the B.Eng. in Electrical/Computer Engineering from the Federal University of Technology, Minna, Nigeria. He received the M.Sc. and Ph.D. degrees from the Obafemi Awolowo University, Ile-Ife, Nigeria. His research interests include research in the fields of computer vision, image processing, signal processing, machine learning, control systems engineering and power systems technology. He serves as a reviewer for several reputable international journals. His research has been published in many reputable international conferences, books, and major international journals. He is a registered Engineer with the Council for the Regulation of Engineering in Nigeria (COREN), a member of the International Association of Engineers (IAENG), and a recipient of the Quarterly Franklin Membership with ID number CR32878 given by the Editorial Board of London Journals Press in 2020 for top quality research output. More recently, his research paper was awarded the best paper of the year 2019 in Cogent Engineering. In addition, he is the recipient of the International Research Award on New Science Inventions (NESIN) under the category of “Best Researcher Award” given by Science Father with ID number 9249, 2020. Currently, he works at Afe Babalola University in the Department of Electrical/Electronics and Computer Engineering. He can be contacted at email: ayodejisalau98@gmail.com.

Dr. Sepiribo Lucky Braide is an Associate Professor in the Department of Electrical Electronics Engineering, Rivers State University, Port Harcourt, Nigeria. He is the past Head of Department, Electrical Engineering from 2018 to 2021, Fellow of the Nigeria Institute of Electrical Electronics Engineers (FNIEEE) and currently the Post Graduate Coordinator in the Department, from 2021 till date. He is a member of several professional bodies/organizations among many includes; Institute of Electrical Electronics Engineers (IEEE), Nigeria Society of Engineers (MNSE), Council for the Regulation of Engineering in Nigeria (COREN), Nigeria Institute of Electrical Electronics Engineers (MNIEEE), International Association of Engineers (MIAENG), He had the following degrees in Electrical Engineering profession which includes; Bachelor of Technology (B.Tech.), Master of Technology (M.Tech.) and Doctor of Philosophy (Ph.D.). He has attended several conferences these includes: ICEPT, NSE, COREN, IEEE, WCECS (San Francisco, USA Oct., 2019), WCE (London UK, July, 2019). His strong pragmatic confrontation to analyses of finding solutions to challenging engineering problems made him compete in many highly reputable international journals, most recently in 2018, International Journal Engineering and Science Invention (IJESI) classified one of his article as Best Paper Award - 2018 certified and titled: *"A Mathematical Model of Double Exponential Wave Shape (Impulse Generator) for Power Sub-station using Laplace Transform"*. He has received so many honors and awards both local and international. He can be contacted at email: sepiribo.braide@ust.edu.ng.

Dr. Aitizaz Ali is a highly respected academic and professional known for his extensive contributions to the fields of artificial intelligence (AI), cybersecurity, and blockchain technology. He holds a distinguished position as a Senior Member of the IEEE, reflecting his significant impact on the global engineering and technology communities. Over the course of his career, He has authored and co-authored more than 100 research papers, establishing himself as a prolific researcher in his domains. His research interests span across several emerging technologies, and his papers have been published in prestigious journals and conferences. His expertise in AI, cybersecurity, and blockchain has earned him recognition as a thought leader in these areas, and his contributions continue to shape the future of these technologies. As a Senior Member of IEEE, he has not only contributed to research but has also been actively involved in various IEEE initiatives, where he shares his knowledge and expertise with the next generation of engineers and researchers. His work and leadership continue to inspire colleagues and students alike, and his commitment to advancing technology remains unwavering. He can be contacted at email: Aitizaz.ali@apu.edu.my.

Dr. Ting Tin Tin received er B.Sc. and Ph.D. in Computer Sciences from University of Science, Malaysia. She joined Gemalto as telecommunication software engineer in Singapore before joined academic industry after her Ph.D. graduation. She has more than 12 years of lecturing, supervising projects, and research. She received her professional certification in project management from PMI and data analytics from SAS. Currently, she is attached to INTI International University responsible primary in research and postgraduate supervision. She is a passionate researcher in her publication collaborate with national and international researchers i.e., Singapore, Bangladesh, India, Nigeria, Pakistan, United Arab Emirates, and Saudi Arabia. Her research interests including big data analytics, information systems engineering, educational data mining, psycho-academic research, and software engineering. She started being active in her research since 2022, increasing her Google Scholar H-index from 1 to 4 (2023). Currently, she is a freelancer serves as freelance lecturer in INTI International University, Monash University, Tunku Abdul Rahman University of Management and Technology, and Methodist College Kuala Lumpur. Her responsibility including Ph.D. students' supervision; master's programme course leader; course leader; delivery, coordination and development of learning materials for undergraduates, setting of examination papers and marking schemes, conduct lecture, tutorial, practical laboratory, mid-term test; open day faculty consultant; final year project supervisor and moderator; research publication. She can be contacted at email: tintin.ting@newinti.edu.my.